



Lab on a Chip

Tumor-on-a-chip: a microfluidic model to study cell response to environmental gradients.

Journal:	<i>Lab on a Chip</i>
Manuscript ID	LC-ART-03-2019-000270.R1
Article Type:	Paper
Date Submitted by the Author:	16-Aug-2019
Complete List of Authors:	<p>Ayuso, Jose; University of Wisconsin, Biomedical Engineering Virumbrales-Munoz, Maria; University of Wisconsin, Biomedical Engineering McMinn, Patrick; University of Wisconsin Madison College of Engineering, Biomedical Engineering Rehman, Shujah; Morgridge Institute for Research Gomez, Ismael; San Carlos Clinic Hospital, Allergy research group - IdISSC.; University Carlos III of Madrid, Materials department Karim, Mohammad; Morgridge Institute for Research Truttschel, Regan; University of Wisconsin, Biomedical Engineering Wisinski, Kari; University of Wisconsin, Biomedical Engineering Beebe, David; University of Wisconsin, Biomedical Engineering Skala, Melissa; University of Wisconsin, Biomedical Engineering; Morgridge Institute for Research</p>

SCHOLARONE™
Manuscripts

Tumor-on-a-chip: a microfluidic model to study cell response to environmental gradients.

Jose M. Ayuso^{1,2,3}, Maria Virumbrales-Munoz^{2,3}, Patrick H. McMinn^{2,3}, Shujah Rehman^{1,2,3}, Ismael Gomez^{4,5}, Mohammad R. Karim^{1,2,3}, Regan Trusttchel^{2,3}, Kari B. Wisinski^{2,3}, David J. Beebe^{2,3,6##}, Melissa C. Skala^{1,2,3##}.

1. Morgridge Institute for Research, 330 N Orchard street, Madison, WI, USA.
2. Department of Biomedical Engineering, University of Wisconsin, Madison, WI, USA.
3. The University of Wisconsin Carbone Cancer Center, University of Wisconsin, Madison, WI, USA.
4. Allergy research group, IdISSC. San Carlos Clinic Hospital, Madrid, Spain.
5. Materials department, Carlos III University. Leganes, Spain.
6. Department of Pathology & Laboratory Medicine, University of Wisconsin, Madison, WI, USA.

* These authors have coordinated this work equally.

Corresponding authors: David J Beebe, djbeebe@wisc.edu. Melissa C Skala, mcskala@wisc.edu.

Abstract

Limited blood supply and rapid tumor metabolism within solid tumors leads to nutrient starvation, waste product accumulation and the generation of pH gradients across the tumor mass. These environmental conditions modify multiple cellular functions, including metabolism, proliferation, and drug response. However, capturing the spatial metabolic and phenotypic heterogeneity of the tumor with classic in vitro models remains challenging. Thus, in this work a microfluidic tumor slice model was developed to study cell behavior under metabolic starvation gradients. The presented microdevice comprises a central chamber where tumor cells were cultured in a 3D collagen hydrogel. A lumen on the flank of the chamber was used to perfuse media, mimicking the vasculature. Under these circumstances, tumor cell metabolism led to the generation of viability, proliferation and pH gradients. The model decoupled the influence of oxygen from other nutrients, revealing that cell necrosis at the core of the model could be explained by nutrient starvation. The microdevice can be disassembled to retrieve the

cells from the desired locations to study molecular adaptations due to nutrient starvation. When exposed to these pH gradients and low nutrient conditions, cancer cells showed multiple changes in their gene expression profile depending on their distance from the lumen. Those cells located further from the lumen upregulated several genes related with stress and survival response, whereas genes related with proliferation and DNA repair were downregulated. This model may help to identify new therapeutic opportunities to target the metabolic heterogeneity observed in solid tumors.

Introduction

Solid tumors are highly heterogeneous and plastic systems¹⁻³. As solid tumors grow, the accelerated tumor metabolism, combined with an insufficient blood supply to support this uncontrolled metabolism, lead to nutrient exhaustion in the tumor microenvironment⁴⁻⁶. Simultaneously, cellular waste products accumulate in the innermost regions of the tumor. In this context, one of the main waste products is lactic acid, which also causes a pH drop at the core of the tumor^{7, 8}. Taken together, this evidence illustrates how tumor cells generate an extremely harsh microenvironment characterized by gradients of nutrient exhaustion, waste product accumulation, and pH across the solid tumor mass^{9, 10}. Thus, tumor cells located nearby blood vessels have enough nutrients to keep growing, forming a proliferative outer perimeter. Conversely, those cells located in the innermost region die of nutrient starvation, generating a necrotic core in the center of the tumor¹¹. However, those cells located between the proliferative rim and the necrotic core play a critical role in tumor development. In this intermediate layer, tumor cells grow in an environment characterized by moderate starvation, hypoxia and acidic pH⁹. Interestingly, there are still some nutrients present, as well as metabolic intermediates, that were not consumed by the proliferative cells at the outer perimeter. Under these circumstances, tumor cells in the intermediate layer adapt their metabolic program to survive within the surrounding harsh

microenvironment¹². Cancer cells decrease or even completely stop their proliferation rate to minimize nutrient consumption, leading to a population of quiescent tumor cells. These quiescent cells activate alternative metabolic pathways and different survival responses (e.g., apoptosis resistance, starvation-induced DNA protection)¹²⁻¹⁶. Quiescent tumor cells can negatively influence patient outcome because they evade most chemotherapy agents (e.g., doxorubicin, paclitaxel, cisplatin), which only target proliferating cells, usually located at the rim of the tumor. Therefore, these quiescent cells inside the tumor may remain impervious to the treatment^{9, 17}. Interestingly, long-term exposure to the chemotherapy drug enables quiescent cells to develop drug resistance mechanisms (e.g., increased drug efflux, blockade of drug uptake proteins, overexpression of detoxifying systems and DNA repair mechanisms or apoptosis evasion)^{9, 18}. Once the outer proliferative rim is destroyed, these chemotherapy-resistant cells are exposed again to high amounts of nutrients, resuming cell proliferation and leading to a chemotherapy drug-resistant relapse^{19, 20}.

In order to find effective therapies capable of targeting these heterogeneous cell populations in the solid tumor, *in vitro* models need to recapitulate the metabolic heterogeneity of the solid tumor microenvironment. In this context, multicellular spheroids represent one of the most traditional 3D *in vitro* models to study solid tumors^{21, 22}. Cancer spheroids exhibit many of the characteristics of solid tumors (e.g., proliferating rim, quiescent region, necrotic core, acidosis, gradients of nutrients)¹¹. However, to generate these gradients and the necrotic core, the spheroid size must be at least a few hundred microns ($\approx 400 \mu\text{m}$), making it inaccessible by most microscopy techniques²³. Another challenge regarding spheroids is the fact that hypoxia and nutrient gradients appear together, which entangles cellular alterations caused by hypoxia and nutrient starvation²⁴. Finally, selectively retrieving the cells from different locations of the spheroid (e.g., proliferating periphery vs quiescent layer) for downstream analysis is extremely challenging²³.

Thus, microfluidic devices are an interesting alternative to more traditional methods to mimic solid tumors²⁵⁻²⁷. In fact, previous studies have demonstrated the capacity of microfluidic devices to generate gradients of oxygen^{28, 29}, nutrients²³, pH³⁰, growth factors³¹⁻³³ and cell viability³⁴. However, none of these models enable selective retrieval of cells from different locations in the microdevice, which is essential to decipher the cellular metabolic adaptations under varying microenvironments. Therefore, here we developed a microfluidic tumor slice model that mimics the nutrient starvation and pH gradients, while allowing for selective retrieval of the cells for downstream analysis. Adjusting the initial cell density, the microdevice generated the proliferating, quiescent, and necrotic regions present in solid tumors. Additionally, polydimethylsiloxane (PDMS) is permeable to oxygen, thus the microdevice provides a method to decouple hypoxia and nutrient starvation. In this context, the results showed that under normoxic conditions, the microenvironment generated inside the microdevice led to the formation of a proliferative, quiescent, and necrotic region across the model. However, the addition of hypoxic conditions led to a moderate increase in the necrosis in the model. Finally, cells from the proliferative and quiescent regions were isolated, revealing multiple adaptations related to cell survival and stress response in the cells located further from the lumen.

Materials and Methods

Microdevice fabrication

The tumor slice microdevice was fabricated using a protocol more specifically detailed in³⁵. In summary, illustrator was used to design the template, which was then fabricated using SU-8 based lithography. The SU-8 template was used to generate the final microdevices by pouring PDMS on top and polymerizing it during 4 hours at 80 °C. Following PDMS polymerization, the microdevices were removed from the SU-8 wafer, and the bottom and top layers of the microdevice were assembled together. This approach yielded a non-permanent bonding between the two layers of PDMS, allowing the disassemble

of the microdevice after the experiments to retrieve the cells. To generate the lumen structure, a 340 μm -diameter PDMS rod was inserted in the chamber. Next, the microdevices were plasma bonded to a 60mm glass bottom Petri dish. Since top and bottom layers were already together, the plasma treatment did not affect the interface between both layers, keeping the bonding reversible. Prior cell culture experiments, microdevices were sterilized through 15 minutes of UV exposure. Then, microdevices were treated with poly(ethyleneimine) (Sigma-Aldrich, 03880) diluted in water at 2% for 10 minutes, followed by 30 minutes with glutaraldehyde (Sigma-Aldrich, G6257) diluted at 0.4% in water to enhance hydrogel attachment.

Glucose diffusion

In order to study the diffusion of nutrients from the lumen into the bulk of the collagen hydrogel, a fluorescent glucose analog, 2-(N-(7-Nitrobenz-2-oxa-1,3-diazol-4-yl)Amino)-2-Deoxyglucose (NBDG) (Thermo Fisher, N13195), was used as an indicator for glucose diffusion kinetics. Briefly, 200 μM NBDG solution was added to the lumen of microdevices containing 4 mg/mL collagen I gels. NBDG diffusion was monitored taken images in a Nikon TiE every 30 minutes for two hours. NBDG diffusion profile was analyzed using FIJI, an open-source image analysis program.

Cell culture

Colon cancer HCT-116 cells (ATCC) were cultured in RPMI 1640 (Thermo Fisher, 21870076) supplemented with 10% FBS (Thermo Fisher, 26140079). To prepare the tumor slice model, HCT-116 cells were trypsinized and resuspended at the desired density. Next, a 4.0 mg/ml collagen hydrogel containing 5, 7.5, 10 or 15 million HCT-116 cells/ml was prepared as follows: 10 μl of 10x PBS, 2.45 μl of 1M NaOH, 97.8 μl of 8.43 mg/ml collagen type I, and 100 μl of cell suspension. The collagen hydrogel was injected into the chamber of the microdevice and polymerized at room temperature for 20 minutes. The

PDMS rod was removed using sterilized tweezers after collagen polymerization. This generated a tunnel in the hydrogel through which media was perfused to nourish the cells. 5 ml of cell culture media was then added to the Petri dish and the devices were placed in an incubator at 37°C with 5% CO₂.

Cell viability

Cell viability was assessed after diluting stock solutions of 5mg/ml calcein acetomethyl ester (CAM) (Thermo Fisher, C3100MP) and 2mg/ml prodidium iodide (PI) (Thermo Fisher, P1304MP) at 1:1000 and 1:500 respectively in PBS. In order to ensure a homogenous staining, the upper half of the microdevice was removed to expose the collagen hydrogel and the CAM/PI solution was added on top for 15 minutes. Subsequently evaluated by fluorescent/confocal imaging using a Leica SP8 3X STED super-resolution confocal microscope.

Modeling and simulation of the cell-glucose interactions (Materials & Methods)

A 1-dimensional model of the microdevice was developed to determine the effect of the diffusion ports on the glucose diffusion and cell survival profile inside the microdevice³⁶. Thus, we performed two computational simulations, based on a partial differential equations model. Both simulations differed on their boundary conditions to reflect the presence (mixed boundary conditions) or absence (Neumann boundary conditions) of such diffusion ports. The in-depth description of the model can be found in the supporting information.

Proliferation analysis

In order to study proliferation, HCT-116 were transiently transduced with the Premo™ FUCCI Cell Cycle Sensor (Thermo, P36237). This cell cycle sensor contains a genetically-modified baculovirus that includes two different reporters coupled to TagRFP and EmGFP that are expressed alternatively during the G1

phase or the S/G2/M phases respectively. This approach labelled proliferating cells in green, whereas non-proliferating cells appear red. Briefly, cells were transduced using a 60 virus particle/cell ratio for 48 hours in 75 μ l in a 96-wellplate. Next, transduced cells were trypsinized, mixed with non-transduced HCT-116 cells in a 1/10 ratio and cultured in the microdevice.

Ph and oxygen profile analysis

The potential presence of pH and oxygen gradients across the microdevice was analyzed using commercially available dyes SNARF-1 AM (C1272, Thermo Fisher) and Image-It hypoxia reagent (H10498, Thermo Fisher) respectively. The compounds were dissolved in DMSO following the supplier instructions. To measure pH, HCT-116 cells were trypsinized, incubated with 10 μ M SNARF-1 AM for 5 min and washed twice with PBS. Then, the cells were cultured in the microdevice and fluorescence was visualized at 500 nm excitation whereas emission was quantified at 580 and 640 nm. The emission ratio between these two wavelengths was used to calculate the pH. The oxygen profile was analyzed using the hypoxia reagent, which increases its fluorescence as oxygen concentration decreases. This compound was added to the cells, as well as to the hydrogel mixture, at 10 μ M. Hypoxia-induced fluorescence was visualized 24 hours later at 488 nm/650 nm excitation/emission.

Cell isolation from the microdevice

In order to selectively retrieve the cell from the microdevice, the upper half of the microdevice was removed to expose the collagen hydrogel. Using a 1 mm-diameter biopsy punch (33-31AA-P/25, Fisher Scientific), a hydrogel punches were obtained at the different locations (i.e., 0, 5 and 10 mm from the lumen). The hydrogel punches were transferred to an Eppendorf tube with 6 mg/ml type I collagenase for 30 seconds to degrade the hydrogel. Next, the cells were centrifuged and resuspended in media to

remove the excess of collagenase. For RT-qPCR experiments, the hydrogel punches were directly treated with lysis buffer to isolate the mRNA.

RT-qPCR

To study how cells adapted to the evolving microenvironment within the tumor slice microdevice, the expression of multiple genes related with different pathways was analyzed by RT-qPCR. Briefly, mRNA was isolated from the different punches using a Dynabeads™ mRNA DIRECT™ Purification Kit (Thermo Fisher, 61011). Isolated mRNA was quantified using a Qubit fluorometer (Thermo Fisher) and a Qubit™ RNA BR Assay Kit (Q10210, Thermo Fisher). mRNA was reverse transcribed to cDNA using the RT2 PreAMP cDNA Synthesis Kit (Qiagen, 330451). cDNA was analyzed by RT-qPCR using a Qiagen RT2 profiler custom panel (Qiagen, PAHS-033Z) and data was analyzed using the Qiagen online software (<http://pcrdataanalysis.sabiosciences.com/pcr/arrayanalysis.php>).

Results

Microdevice operation and cell culture

During tumor development, cancer cell metabolism generates a complex microenvironment characterized by nutrient starvation, waste product accumulation and pH gradients. The combination of these environmental factors lead to the formation of different phenotypes across the tumor mass (Figure 1A). A microfluidic tumor-on-a-chip model was fabricated to mimic this environment. The microdevice comprised a rectangular microchamber with a PDMS rod in one of the sides to generate a lumen perfused with culture medium (Figure 1B-C). HCT-116 colon cancer cells were mixed with the collagen solution and injected into the microchamber through the hydrogel loading port. After collagen polymerization, the PDMS rod was removed, generating a lumen to perfuse culture medium. Given the large dimensions of the chamber (15 mm L x 10 mm W), two series of parallel small ports were included

on the upper half of the microdevice on both sides of the lumen (Figure 1B). In the absence of these ports and culture medium flow, nutrient diffusion from the hydrogel loading ports did not suffice to maintain the cells alive, leading to cell death across all the chamber (Supporting Figure 1). Diffusion ports ensured that nutrients diffused homogeneously across the chamber, keeping those cells next to the lumen alive. Additionally, this approach avoided the use of external pumps to flow culture medium through the lumen, making the design more accessible to potential users. Computational simulations showing the glucose and cell viability profile also highlighted the impact of the diffusion ports (Supporting figure 1). In this context, the simulation showed that in the absence of diffusion ports, there was no glucose gradient, and cells reached a stationary state of cell death across the chamber. On the other hand, the presence of diffusion ports led to a glucose gradient descending to a stationary state on the right side of the chamber, generating three different cell populations (i.e., proliferating, stationary, and dead cells) across the chamber (Supporting Figure 1).

Additionally, the large dimensions of the central chamber (i.e., 15 mm L x 10 mm L) favored a slow nutrient penetration in the furthest regions of chamber, illustrated by the diffusion profile of the fluorescent glucose analog NBDG (Supporting Figure 2). After 24 hours in culture, cell viability was evaluated by confocal microscopy staining of viable and dead cells in green (CAM) and red (PI), respectively. The confocal images showed a gradient of cell viability across the chamber width (Figure 1D). The two halves of the PDMS microdevice can be separated to expose the hydrogel and retrieve the cells after the experiments for downstream analysis (Figure 1E).

Figure 1 Microdevice design and operation. A) Schematic representation of the different tumor phenotypes generated in a solid tumor due to nutrient starvation. B) Scheme of the tumor slice microdevice showing the central microchamber (10 mm L x 15 mm W x 0.5 mm H), the lumen (350 μ m diameter) and the different loading and diffusion ports. The bottom panel shows the microdevice cross-section. HCT-116 cells were embedded in a collagen hydrogel, the lumen, as well as the pores in the upper half, allow nutrient diffusion. C) Picture of the microdevice filled with blue and red-colored water for visualization purposes. D) Confocal image showing HCT-116 cell viability after 24 hours in the microdevice at 10 million cells/ml. Viable and dead cells are shown in green (CAM) and red (PI) respectively. White dashed line indicates the lumen position.

E) Scheme illustrating the protocol to retrieve the cells from the device. Both halves are disassembled, exposing the collagen hydrogel and then hydrogel punches are isolated using a biopsy puncher.

Next, we evaluated the cell density required to stress the cells while keeping most of them alive (Figure 2A). When cultured at 15 million cells/ml, HCT-116 cells generated a large necrotic region in the middle of the chamber with a well-defined live-dead transition zone (Figure 2B and E). This result confirmed that a necrotic region could be generated in the microdevice. However, the necrotic region occupied a large area of the microdevice (>50%), limiting the area to extract viable cells. Thus, the cell density was reduced by half in order to decrease cell mortality and increase the area of the chamber with live cells. When cultured at 7.5 million cells/ml, the necrotic region generated was smaller (<25%) and it almost disappeared at 5 million cells/ml, generating only a minor necrosis (<5%) (Figure 2C-G).

Figure 2 Cell density modulates the necrotic region generation. A) HCT-116 cells cultured in the microdevice at different densities to evaluate the effect of cell density on the necrotic region generation. B) HCT-116 at 15 million cells/ml. After 24 hours cell viability was evaluated staining viable and dead cells in green (CAM) and red (PI) respectively. The confocal image showed the formation of a large necrotic region with a dense necrotic area in the middle of the chamber. White dashed line indicates the lumen position. C) HCT-116 cells at 7.5 million cells/ml. The results showed the generation of a smaller necrotic region. D) HCT-116 cells at 5 million/ml. The viability staining showed no necrotic region formation. E) inserts showing a magnification of the yellow rectangles in the confocal images to illustrate the change in cell viability. F-G) graphs show the fluorescence intensity profile of the viable and necrotic cells across the chamber width at the different densities.

We next investigated whether nutrient starvation led to a proliferation gradient at 5 million cells/ml. HCT-116 cells were transduced with the fluorescent reporter Premo FUCCI, labelling proliferating and non-proliferating cells in green and red respectively (Figure 3A). During the transition from G1 phase to S phase, cells appear both red and green, generating a yellow fluorescence that gradually changes as the cell moves through the cell cycle. To visualize individual cells, only 10% of the cells injected in the device were transduced with the reporter (Figure 3B and D). Heterogeneity in the transfection efficiency led to different levels of reporter expression in the transfected cells. Despite this heterogeneity, fluorescence

microscopy revealed the presence of transfected cells across all the hydrogel thickness (Supporting figure 3 and Supporting movie 1). The distribution analysis revealed most of the proliferating cells were located in the first 2 mm of the chamber, whereas the number of proliferating cells decreased as the distance from the lumen increased (Figure 3D). This experiment demonstrated that, at 5 million cells/ml, the metabolic environment generated inside of the microdevice already triggered a cell response. Additionally, proliferation and viability gradients are commonly observed *in vivo*. To explore whether proliferation and viability gradients could be simultaneously generated in the microfluidic device, the proliferation analysis was also performed at 15 million cells/ml (Figure 3C and D). The results showed that when cultured at 15 million cells/ml, HCT-116 cells generated a gradient of proliferation as well as cell viability.

Figure 3. Cell proliferation. A) HCT-116 cells were transduced with the premo FUCCI sensor, a fluorescent reporter that fluoresces in red when cells are in G1 phase and green during S/G2/M phase. Transduced HCT-116 cells were cultured in the microdevice for 24 hours and then imaged. B) Confocal images showing the proliferating (in green) and non-proliferating (in red) cells inside the culture chamber after 24 hours at 5 million cells/ml. C) Confocal images showing the proliferating (in green) and non-proliferating (in red) cells inside the culture chamber after 24 hours at 15 million cells/ml. D) The graph shows the percentage of proliferating (in green) and non-proliferating (in red) cells. Images shown in B and C were divided in 10 vertical regions of interest of 1 mm width. The ratio of proliferating (G2/S/M phase) vs non-proliferating (G1 phase) and proliferating cells per region was quantified. Asterisks denote p-value < 0.05.

Presence of pH gradients across the tumor slice model

Different characteristics of the tumor microenvironment (TME) were then investigated. Specifically, pH evolution across the chamber was characterized. We used SNARF-1 AM, a colorless compound that turns fluorescence once it is inside of the cells. The SNARF-1 spectrum depends on pH, and green-shifts as the pH decreases from neutral to acidic. To test the sensitivity of SNARF-1 AM, HCT-116 cells were seeded on Petri dishes in 2D and stained with SNARF-1 AM. Next, the cells were treated with Nigericin, which acts as a H^+ and K^+ transporter, balancing the extracellular and intracellular pH. The cells were cultured in PBS solutions at different pH and intra and extracellular pH equilibrated due to the Nigericin. Confocal microscopy revealed intracellular SNARF-1 changed color when the cells were cultured in the

different pH solutions (Figure 4A). This color change was quantified by plotting the 580/640 nm emission ratio, which generates a linear correlation in the range analyzed (6.31-7.83 pH) (Figure 4B). HCT-116 cells were cultured at 5 and 10 million cells/ml and the pH profile was analyzed after 24 hours to evaluate the effect of the cell density on the pH profile. When cultured at 5 million cells/ml, HCT-116 cells generated a gradient of pH across the chamber width, becoming more acidic as the distance from the lumen and the ports increased (Figure 4C and D). Cultured at 10 million cell/ml, HCT-116 cells generated a gradient that showed a faster decrease in pH and reached a plateau phase at 4 mm (Figure 4C and D). These results demonstrated that even at 5 million cells/ml, when no necrotic core was observed, pH gradients were already present in the microdevice. Additionally, the shape of the pH profile could be modulated by changing the initial cell density.

Figure 4 pH profile. A) HCT-116 were cultured in 2D at different pH and stained with the pH sensor SNARF-1 AM. SNARF-1 AM fluorescence was detected at 580 (green channel) and 640 nm (red channel) and the overlay is shown. The images demonstrated a change in the 580/640 nm ratio at different pH conditions. B) Graph showing the 580/640 nm ratio at different pH. C) HCT-116 cells were cultured at 5 and 10 million cells/ml in the microdevice with the SNARF-1 AM. Fluorescence at 580 and 640 nm was observed after 24 hours. D) The graph shows the estimated pH across the yellow rectangle in the images shown in (C). The estimation was performed using the calibration curve obtained in (B).

Oxygen profile across the tumor slice model

The oxygen profile across the microdevice was then evaluated to assess whether hypoxia was contributing to the generation of the necrotic region. HCT-116 cells were cultured at the highest density tested (i.e., 15 million cells/ml) and stained with a live-dead stain (Figure 5A) to demonstrate the presence of the necrotic region at this cell density. In a similar experiment, cells were stained with an oxygen sensor that increases its yellow fluorescence as oxygen tension decreases, providing a real-time indicator of the oxygen profile across the tumor slice microdevice. The cells were also stained with an infrared dye (vibrant DiD) to evaluate the cell density across the hydrogel, and after 24 hours in culture

the oxygen profile was evaluated by confocal microscopy (Figure 5B and C). The images revealed that the hypoxia signal was low and constant throughout the chamber, demonstrating the absence of an oxygen gradient even at the highest cell density analyzed (Figure 5D). Thus, this result suggested that hypoxia was not the main driving factor in the generation of the necrotic region.

Figure 5. Oxygen profile across the tumor slice model. A) 15 million HCT-116 cells/ml were cultured in the microdevice and 24 hours later cell viability was evaluated. The image shows the formation of the necrotic region at 15 million cells/ml. B-C) In a similar experiment, HCT-116 cells were stained with the cell membrane dye DiO Vybrant (shown in purple) and the hypoxia-sensing dye (yellow) in the microdevice. After 24 hours in culture, the hypoxia sensing dye exhibited a minor fluorescence (in yellow). D) The graph shows the Vybrant and the hypoxia-sensing dye fluorescence profile across the yellow rectangle. The results showed the absence of an oxygen gradient at 15 million cells/ml, whereas the Vybrant dye demonstrated cell density was homogenous across the microdevice.

Additionally, since PDMS is permeable to gas, the oxygen concentration in the chamber can be controlled by adjusting the oxygen tension in the surrounding environment. Thus, the microdevices were cultured in an incubator with controlled oxygen tension to study cell response to different oxygen concentrations. Interestingly, 24 hours under hypoxia conditions (1% O₂) led to a moderate increase in the dead cell profile in the furthest region from the lumen (Figure 6A and B). These results suggested oxygen played a secondary role, while other factors (e.g., pH, nutrient starvation, waste product accumulation) drove the generation of the necrotic region. Additionally, this experiment showed the potential of the device to decouple nutrient starvation from hypoxia.

Figure 6. Influence of hypoxia on the viability gradient. A) HCT-116 cells were cultured at 5 million cells/ml under normoxia (i.e., 20% O₂) and hypoxia (i.e., 1% O₂) for 24 hours. Cell viability was evaluated by staining viable cells in green and dead cells in red. B) Graphs show the viability and mortality profile across the yellow rectangle under normoxia and hypoxia conditions. Culture under hypoxia induced a moderate increase in cell mortality at the furthest region from the device.

Gene expression profile across the tumor slice model

The previous experiments showed the capacity of the microdevice to generate gradients of viability, pH, and proliferation; mimicking some of the metabolic and phenotypic hallmarks of solid tumors. The previous results showed that 5 million cells/ml generated gradients of proliferation and pH while cells remain alive across all the chamber for further isolation. Thus, we seeded HCT-116 cells at 5 million cells/ml and proceeded to retrieve the cells from different locations within the microdevice to study tumor adaptation. HCT-116 cells were cultured in the device at 5 million cells/ml and after 24 hours the upper layer of the microdevice was removed, exposing the hydrogel. Using a biopsy punch (1 mm diameter), fragments of the hydrogel were isolated at different distances from the lumen (0, 5, and 10 mm distance) (Figure 7A). The hydrogel punches were degraded with collagenase and cell viability was evaluated. The results showed how cells next to the lumen and at 10 mm from the lumen exhibited high viability (Figure 7B and C), in agreement with the viability analysis in Figures 2F and G. Then, mRNA was isolated to evaluate gene expression. Multiple genes involved in different cell functions were analyzed (Figure 7D and E and Supporting figure 4). The results showed cells adapted their gene expression depending on their location within the tumor slice microdevice (genes showing significant changes and their functions are summarized in Table 2). Cells located further from the lumen showed upregulation of genes involved in apoptosis resistance (e.g., BIRC3), starvation-induced DNA damage (e.g., GADD45G) and stress response (e.g., ADM). Genes related with cell proliferation showed a significant downregulation in cells further from the lumen, which was in good agreement with the proliferation analysis performed in Figure 3D. Interestingly, multiple genes related with DNA stability and telomere integrity were downregulated in cells further from the lumen, which has been associated with cell senescence and increased mutagenesis.

Figure 7. Spatially-controlled cell isolation and gene profiling. A) HCT-116 cells were cultured in the device at 5 million cells/ml. The modular nature of the device allowed disassembly of the top and bottom halves, exposing the hydrogel with the cells. Using a biopsy punch (1 mm diameter), fragments of the hydrogel were isolated at 0, 5 and 10 mm from the lumen. B) Hydrogel punches were degraded by collagenase type 1 in 1 min and viable and dead cells were immediately stained in green (CAM) and red (PI) respectively. C) The graph shows cell viability was larger than 90% at 0 and 10 mm immediately after recovering the cells. D) The gene expression of ninety genes was analyzed at the three different location (i.e., 0, 5 and 10 mm from the lumen) and the data was analyzed by a non-hierarchical clustering, displaying the data as a

heat-map with dendrograms. The analysis revealed the punches at 5 and 10 mm were more similar compared with the 0 mm punch. E) The waterfall graph shows the fold change normalized mRNA expression for the genes differentially expressed at 0, 5 and 10 mm (blue, green and red).

Finally, several genes associated with the radiation-induced DNA damage repair system were downregulated (e.g., DDB2, ERCC3, and LIG4). The downregulation of these genes may leave these cells located at the furthest regions from the lumen vulnerable to radiation therapies. In conclusion, the metabolic environment created across the tumor slice model led to multiple gene changes that may increase resistance to conventional therapies based on anti-proliferative agents. However, the model identified vulnerabilities in these starved cells that could be targeted with alternative therapies.

Discussion

Traditional cancer chemotherapy is based on compounds that block cell division (e.g., doxorubicin, cisplatin), which induce apoptosis in proliferating tumor cells.²⁰ However, solid tumors are highly heterogeneous structures where gradients of nutrients, pH or waste products play a critical role in drug response⁹. As new therapies become more selective, there is an increasing need for better models that capture this tumor complexity². The model presented here mimics the three characteristic regions observed in solid tumors (i.e., necrotic core, quiescent middle layer, and proliferating perimeter). Additionally, different cell densities were tested in the microdevice to show its capacity to mimic different scenarios (i.e., presence vs absence of the necrotic core). In this context, 15 million cells/ml led to the generation of a necrotic core and gradients of pH and proliferation. On the other hand, when cultured at 5 million cells/ml, most of the cells survived whereas gradients of pH and proliferation were still present. Thus, we decided to isolate the cells from the system at 5 million cells/ml to study how live cells adapted to microenvironment generated inside of the microfluidic device. Whereas many microfluidic devices impose gradients of specific compounds, this model uses the cancer cells to self-generate the metabolic gradients^{28, 37, 38}. Additionally, multiple papers have reported microdevices that impose oxygen gradients, revealing many of the adaptations triggered by hypoxia gradients^{37, 39}. However,

most models that generate nutrient gradients also lead to oxygen gradients (e.g., tumor spheroids). The model presented in this work decoupled these factors, providing metabolic gradients for study under externally controlled oxygen conditions. In the future, this newly characterized model could identify novel metabolic vulnerabilities to tumor cells across multiple microenvironments ⁴⁰.

Conclusion

Nutrient starvation plays a critical role in solid tumors, leading to the generation of different cell populations inside the tumor mass. The microfluidic tumor slice model presented here mimics the characteristic architecture of solid tumors: a proliferative outer perimeter, a quiescent intermediate layer, and the necrotic core at the center. The model showed this organization could be explained by nutrient starvation and pH gradients, suggesting hypoxia can play a secondary role. Finally, retrieving the cells from different locations within the tumor slice model provided insight into starvation-induced cell adaptations, which could lead to novel therapies against solid tumors.

Acknowledgments

University of Wisconsin Carbone Cancer Center (AAB7173). Morgridge Research Institute. NIH grants R01 CA164492, R01 CA185747, R01 CA205101, and NSF grant CBET-1642287.

Conflict of interests

David J. Beebe holds equity in Bellbrook Labs LLC, Tasso Inc., Turba LLC, Salus Discovery LLC, Stacks to the Future LLC, Lynx Biosciences, Inc. and Onexio Biosystems LLC.

References

1. M. R. Junttila and F. J. de Sauvage, *Nature*, 2013, 501, 346-354.
2. Y. Yuan, *Cold Spring Harb Perspect Med*, 2016, 6.
3. F. Runa, S. Hamalian, K. Meade, P. Shisgal, P. C. Gray and J. A. Kelber, *Current molecular biology reports*, 2017, 3, 218-229.
4. C. Garcia-Jimenez and C. R. Goding, *Cell metabolism*, 2019, 29, 254-267.
5. V. Gouirand, F. Guillaumond and S. Vasseur, *Frontiers in oncology*, 2018, 8, 117.
6. R. J. DeBerardinis and N. S. Chandel, *Sci Adv*, 2016, 2, e1600200.
7. S. Romero-Garcia, M. M. Moreno-Altamirano, H. Prado-Garcia and F. J. Sanchez-Garcia, *Frontiers in immunology*, 2016, 7, 52.
8. F. Hirschhaeuser, U. G. Sattler and W. Mueller-Klieser, *Cancer Res*, 2011, 71, 6921-6925.
9. X. Zhang, A. de Milito, M. H. Olofsson, J. Gullbo, P. D'Arcy and S. Linder, *International journal of molecular sciences*, 2015, 16, 27313-27326.
10. J. Goldsmith, B. Levine and J. Debnath, *Methods in enzymology*, 2014, 542, 25-57.
11. A. S. Nunes, A. S. Barros, E. C. Costa, A. F. Moreira and I. J. Correia, *Biotechnol Bioeng*, 2019, 116, 206-226.
12. L. Sun, C. Suo, S. T. Li, H. Zhang and P. Gao, *Biochimica et biophysica acta. Reviews on cancer*, 2018, 1870, 51-66.
13. G. Gentric, V. Mieulet and F. Mechta-Grigoriou, *Antioxidants & redox signaling*, 2017, 26, 462-485.
14. M. Robertson-Tessi, R. J. Gillies, R. A. Gatenby and A. R. Anderson, *Cancer Res*, 2015, 75, 1567-1579.
15. E. C. Nakajima, C. Laymon, M. Oborski, W. Hou, L. Wang, J. R. Grandis, R. L. Ferris, J. M. Mountz and B. Van Houten, *Plos One*, 2014, 9, e102452.
16. R. Lamb, B. Ozsvari, G. Bonuccelli, D. L. Smith, R. G. Pestell, U. E. Martinez-Outschoorn, R. B. Clarke, F. Sotgia and M. P. Lisanti, *Oncotarget*, 2015, 6, 21892-21905.
17. J. Hirpara, J. Q. Eu, J. K. M. Tan, A. L. Wong, M. V. Clement, L. R. Kong, N. Ohi, T. Tsunoda, J. Qu, B. C. Goh and S. Pervaiz, *Redox biology*, 2018, DOI: 10.1016/j.redox.2018.101076, 101076.
18. M. Millard, I. Yakavets, V. Zorin, A. Kulmukhamedova, S. Marchal and L. Bezdetsnaya, *International journal of nanomedicine*, 2017, 12, 7993-8007.
19. A. G. Smith and K. F. Macleod, *The Journal of pathology*, 2018, DOI: 10.1002/path.5222.
20. F. M. Vallette, C. Olivier, F. Lezot, L. Oliver, D. Cochonneau, L. Lalier, P. F. Cartron and D. Heymann, *Biochemical pharmacology*, 2018, DOI: 10.1016/j.bcp.2018.11.004.
21. A. Gorkach and H. Acker, *Biochimica et biophysica acta*, 1994, 1227, 105-112.
22. G. Mehta, A. Y. Hsiao, M. Ingram, G. D. Luker and S. Takayama, *J Control Release*, 2012, 164, 192-204.
23. J. M. Ayuso, M. Virumbrales-Munoz, A. Lacueva, P. M. Lanuza, E. Checa-Chavarria, P. Botella, E. Fernandez, M. Doblare, S. J. Allison, R. M. Phillips, J. Pardo, L. J. Fernandez and I. Ochoa, *Sci Rep*, 2016, 6, 36086.
24. S. Riffle and R. S. Hegde, *Journal of experimental & clinical cancer research : CR*, 2017, 36, 102.
25. S. J. Hachey and C. C. W. Hughes, *Lab on a chip*, 2018, 18, 2893-2912.
26. V. S. Shirure, Y. Bi, M. B. Curtis, A. Lezia, M. M. Goedegebuure, S. P. Goedegebuure, R. Aft, R. C. Fields and S. C. George, *Lab on a chip*, 2018, 18, 3687-3702.
27. H. F. Tsai, A. Trubelja, A. Q. Shen and G. Bao, *Journal of the Royal Society, Interface*, 2017, 14.

28. L. Orcheston-Findlay, A. Hashemi, A. Garrill and V. Nock, *Microelectron Eng*, 2018, 195, 107-113.
29. J. M. Ayuso, R. Monge, A. Martinez-Gonzalez, M. Virumbrales-Munoz, G. A. Llamazares, J. Berganzo, A. Hernandez-Lain, J. Santolaria, M. Doblare, C. Hubert, J. N. Rich, P. Sanchez-Gomez, V. M. Perez-Garcia, I. Ochoa and L. J. Fernandez, *Neuro-Oncology*, 2017, 19, 503-513.
30. C. L. Walsh, B. M. Babin, R. W. Kasinskas, J. A. Foster, M. J. McGarry and N. S. Forbes, *Lab on a chip*, 2009, 9, 545-554.
31. B. J. Kim, P. Hannanta-Anan, M. Chau, Y. S. Kim, M. A. Swartz and M. M. Wu, *Plos One*, 2013, 8.
32. J. M. Ayuso, H. A. Basheer, R. Monge, P. Sanchez-Alvarez, M. Doblare, S. D. Shnyder, V. Vinader, K. Afarinkia, L. J. Fernandez and I. Ochoa, *Plos One*, 2015, 10.
33. J. D. Wu, X. Wu and F. Lin, *Lab on a chip*, 2013, 13, 2484-2499.
34. R. Derda, A. Laromaine, A. Mammoto, S. K. Y. Tang, T. Mammoto, D. E. Ingber and G. M. Whitesides, *Proceedings of the National Academy of Sciences of the United States of America*, 2009, 106, 18457-18462.
35. J. A. Jimenez-Torres, S. L. Peery, K. E. Sung and D. J. Beebe, *Advanced healthcare materials*, 2016, 5, 198-204.
36. J. M. Ayuso, A. Gillette, K. Lugo-Cintrón, S. Acevedo-Acevedo, I. Gomez, M. Morgan, T. Heaster, K. B. Wisinski, S. P. Palecek, M. C. Skala and D. J. Beebe, *EBioMedicine*, 2018, 37, 144-157.
37. Y. A. Chen, A. D. King, H. C. Shih, C. C. Peng, C. Y. Wu, W. H. Liao and Y. C. Tung, *Lab on a chip*, 2011, 11, 3626-3633.
38. S. Kim, H. J. Kim and N. L. Jeon, *Integrative biology : quantitative biosciences from nano to macro*, 2010, 2, 584-603.
39. X. Lin, Q. Chen, W. Liu, J. Zhang, S. Wang, Z. Lin and J. M. Lin, *Sci Rep*, 2015, 5, 9643.
40. S. H. Shahruzaman, S. Fakurazi and S. Maniam, *Cancer management and research*, 2018, 10, 2325-2335.

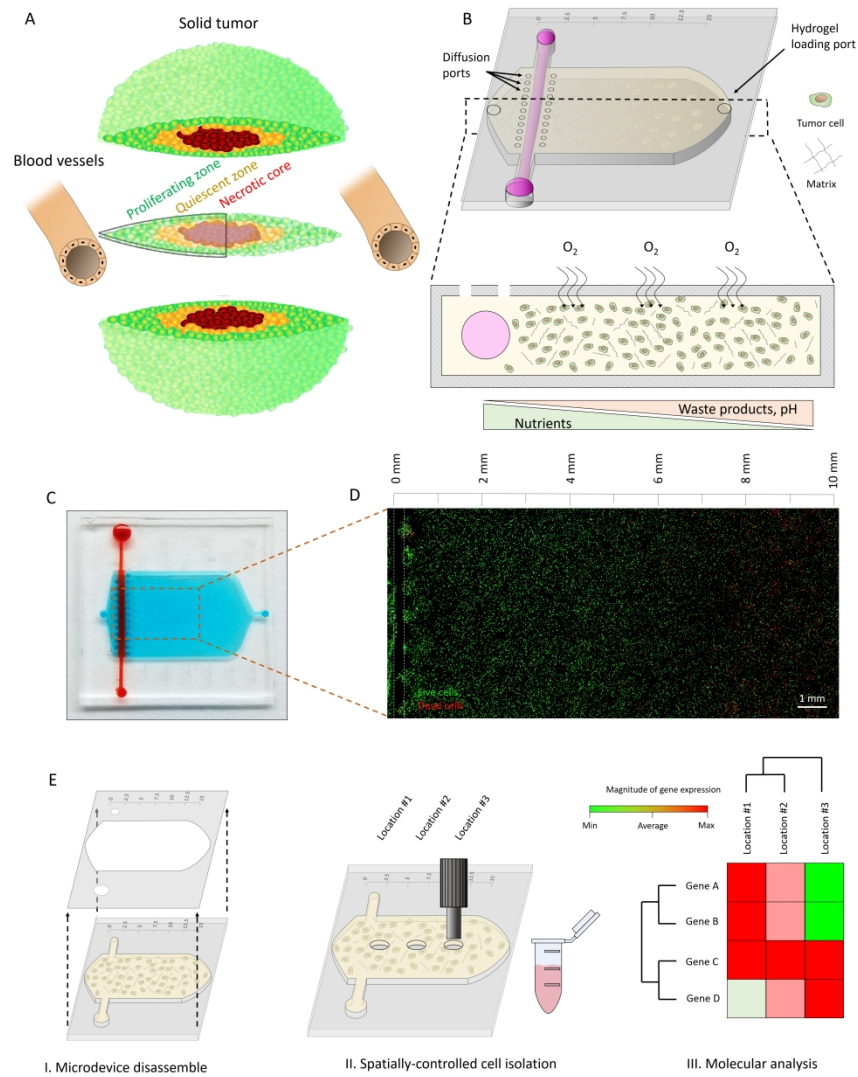


Figure 1 Microdevice design and operation. A) Schematic representation of the different tumor phenotypes generated in a solid tumor due to nutrient starvation. B) Scheme of the tumor slice microdevice showing the central microchamber (10 mm L x 15 mm W x 0.5 mm H), the lumen (350 μ m diameter) and the different loading and diffusion ports. The bottom panel shows the microdevice cross-section. HCT-116 cells were embedded in a collagen hydrogel, the lumen, as well as the pores in the upper half, allow nutrient diffusion. C) Picture of the microdevice filled with blue and red-colored water for visualization purposes. D) Confocal image showing HCT-116 cell viability after 24 hours in the microdevice at 10 million cells/ml. Viable and dead cells are shown in green (CAM) and red (PI) respectively. White dashed line indicates the lumen position. E) Scheme illustrating the protocol to retrieve the cells from the device. Both halves are disassembled, exposing the collagen hydrogel and then hydrogel punches are isolated using a biopsy puncher.

755x889mm (150 x 150 DPI)

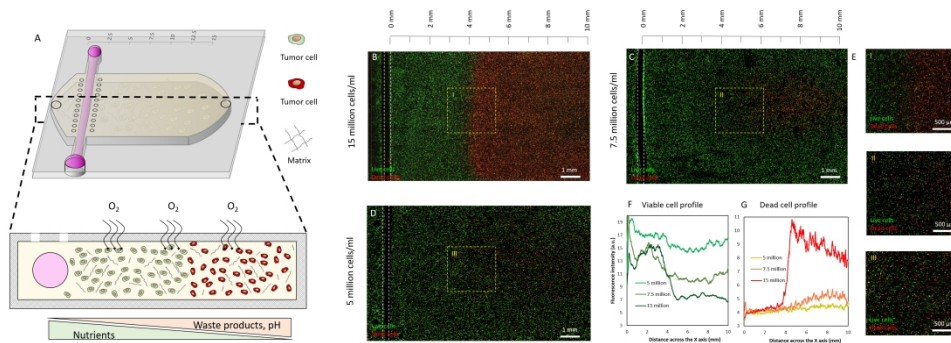


Figure 2 Cell density modulates the necrotic region generation. A) HCT-116 cells cultured in the microdevice at different densities to evaluate the effect of cell density on the necrotic region generation. B) HCT-116 at 15 million cells/ml. After 24 hours cell viability was evaluated staining viable and dead cells in green (CAM) and red (PI) respectively. The confocal image showed the formation of a large necrotic region with a dense necrotic area in the middle of the chamber. White dashed line indicates the lumen position. C) HCT-116 cells at 7.5 million cells/ml. The results showed the generation of a smaller necrotic region. D) HCT-116 cells at 5 million/ml. The viability staining showed no necrotic region formation. E) inserts showing a magnification of the yellow rectangles in the confocal images to illustrate the change in cell viability. F-G) graphs show the fluorescence intensity profile of the viable and necrotic cells across the chamber width at the different densities.

643x238mm (150 x 150 DPI)

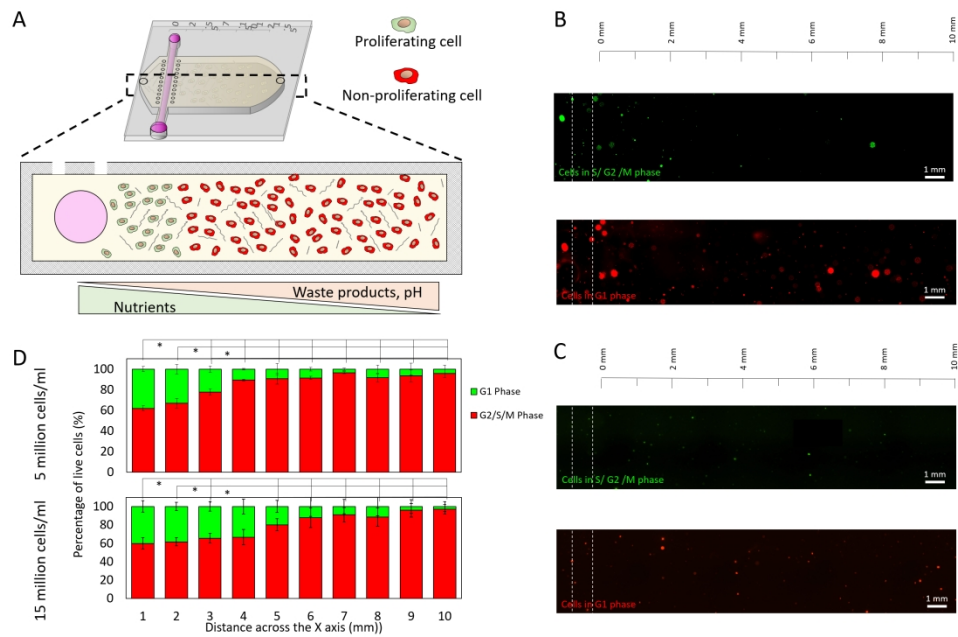


Figure 3. Cell proliferation. A) HCT-116 cells were transduced with the premo FUCCI sensor, a fluorescent reporter that fluoresces in red when cells are in G1 phase and green during S/G2/M phase. Transduced HCT-116 cells were cultured in the microdevice for 24 hours and then imaged. B) Confocal images showing the proliferating (in green) and non-proliferating (in red) cells inside the culture chamber after 24 hours at 5 million cells/ml. C) Confocal images showing the proliferating (in green) and non-proliferating (in red) cells inside the culture chamber after 24 hours at 15 million cells/ml. D) The graph shows the percentage of proliferating (in green) and non-proliferating (in red) cells. Images shown in B and C were divided in 10 vertical regions of interest of 1 mm width. The ratio of proliferating (G2/S/M phase) vs non-proliferating (G1 phase) and proliferating cells per region was quantified. Asterisks denote p-value < 0.05.

517x351mm (150 x 150 DPI)

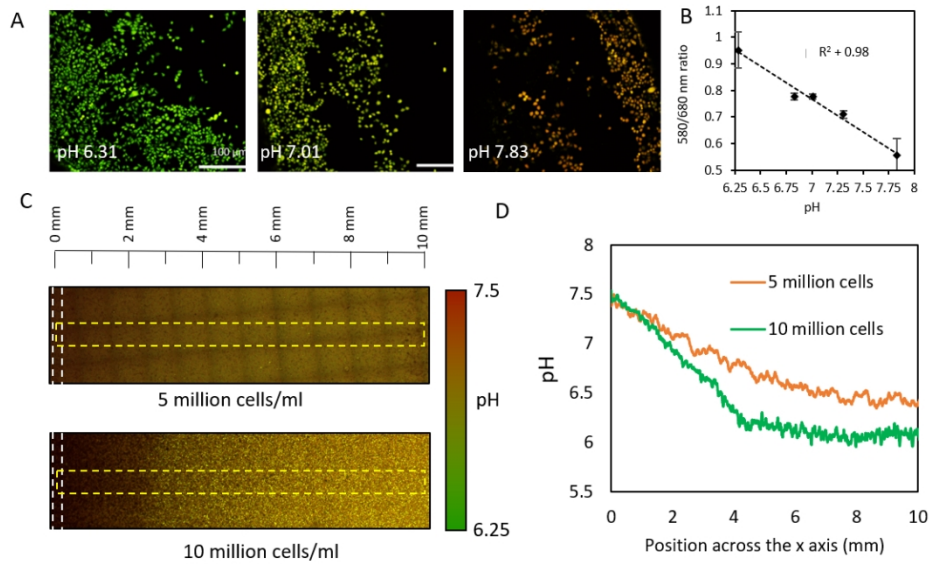


Figure 4 pH profile. A) HCT-116 were cultured in 2D at different pH and stained with the pH sensor SNARF-1 AM. SNARF-1 AM fluorescence was detected at 580 (green channel) and 640 nm (red channel) and the overlay is shown. The images demonstrated a change in the 580/640 nm ratio at different pH conditions. B) Graph showing the 580/640 nm ratio at different pH. C) HCT-116 cells were cultured at 5 and 10 million cells/ml in the microdevice with the SNARF-1 AM. Fluorescence at 580 and 640 nm was observed after 24 hours. D) The graph shows the estimated pH across the yellow rectangle in the images shown in (C). The estimation was performed using the calibration curve obtained in (B).

202x127mm (150 x 150 DPI)

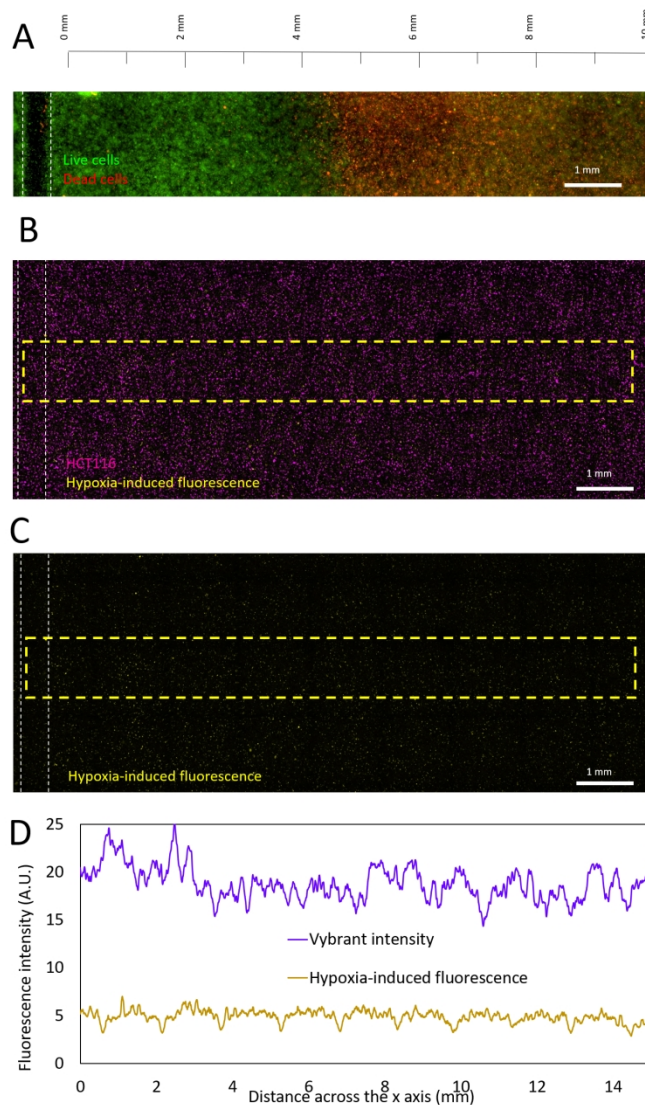


Figure 5. Oxygen profile across the tumor slice model. A) 15 million HCT-116 cells/ml were cultured in the microdevice and 24 hours later cell viability was evaluated. The image shows the formation of the necrotic region at 15 million cells/ml. B-C) In a similar experiment, HCT-116 cells were stained with the cell membrane dye DiO Vybrant (shown in purple) and the hypoxia-sensing dye (yellow) in the microdevice. After 24 hours in culture, the hypoxia sensing dye exhibited a minor fluorescence (in yellow). D) The graph shows the Vybrant and the hypoxia-sensing dye fluorescence profile across the yellow rectangle. The results showed the absence of an oxygen gradient at 15 million cells/ml, whereas the Vybrant dye demonstrated cell density was homogenous across the microdevice.

267x426mm (150 x 150 DPI)

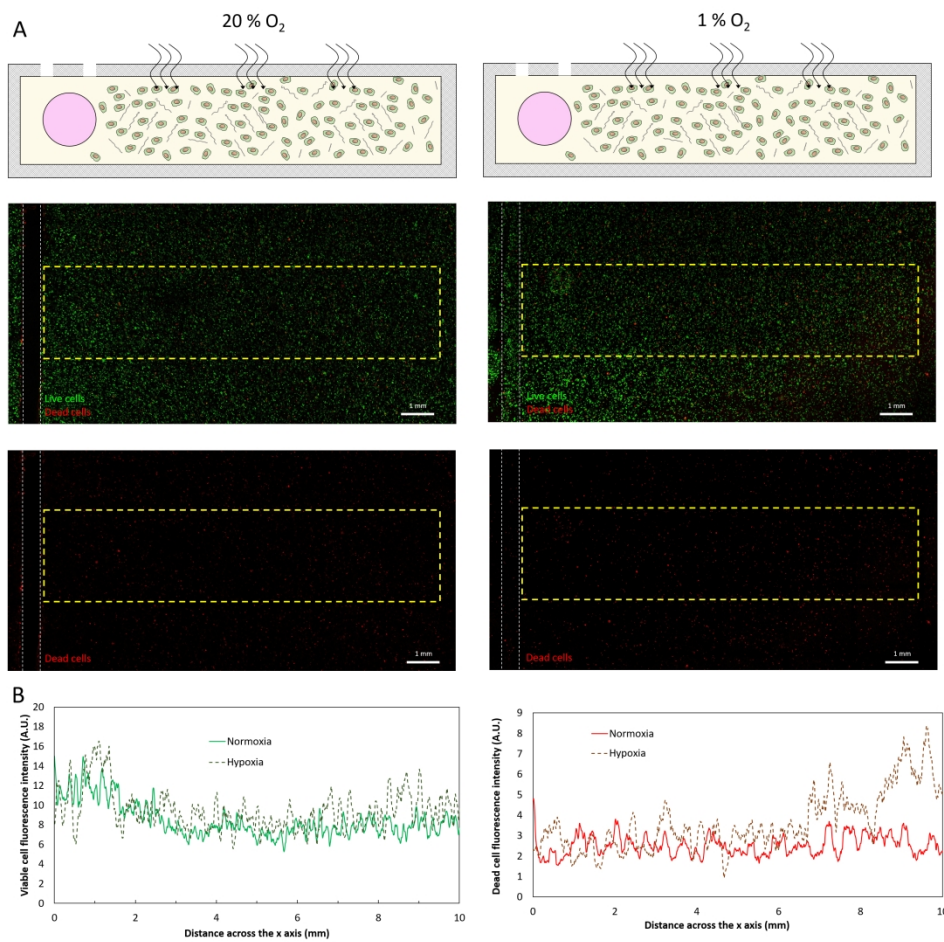


Figure 6. Influence of hypoxia on the viability gradient. A) HCT-116 cells were cultured at 5 million cells/ml under normoxia (i.e., 20% O₂) and hypoxia (i.e., 1% O₂) for 24 hours. Cell viability was evaluated by staining viable cells in green and dead cells in red. B) Graphs show the viability and mortality profile across the yellow rectangle under normoxia and hypoxia conditions. Culture under hypoxia induced a moderate increase in cell mortality at the furthest region from the device.

566x551mm (150 x 150 DPI)

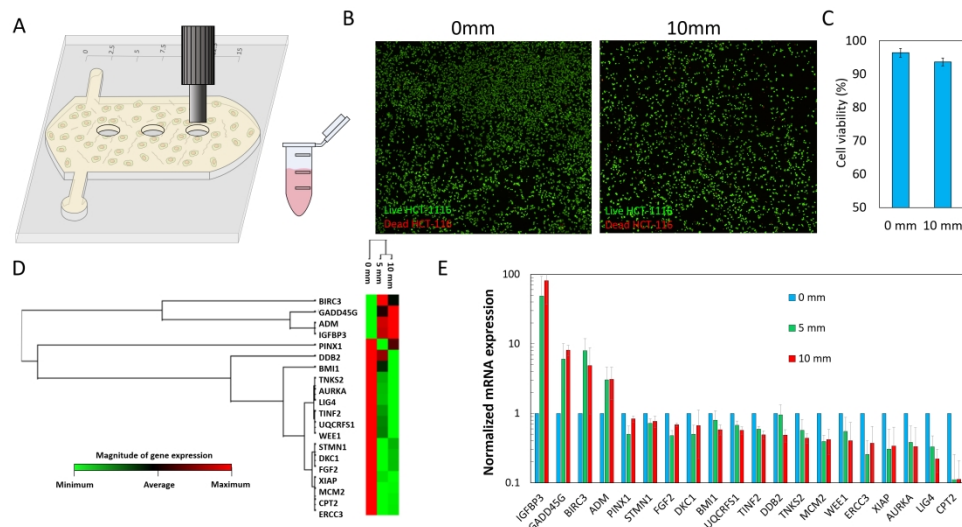
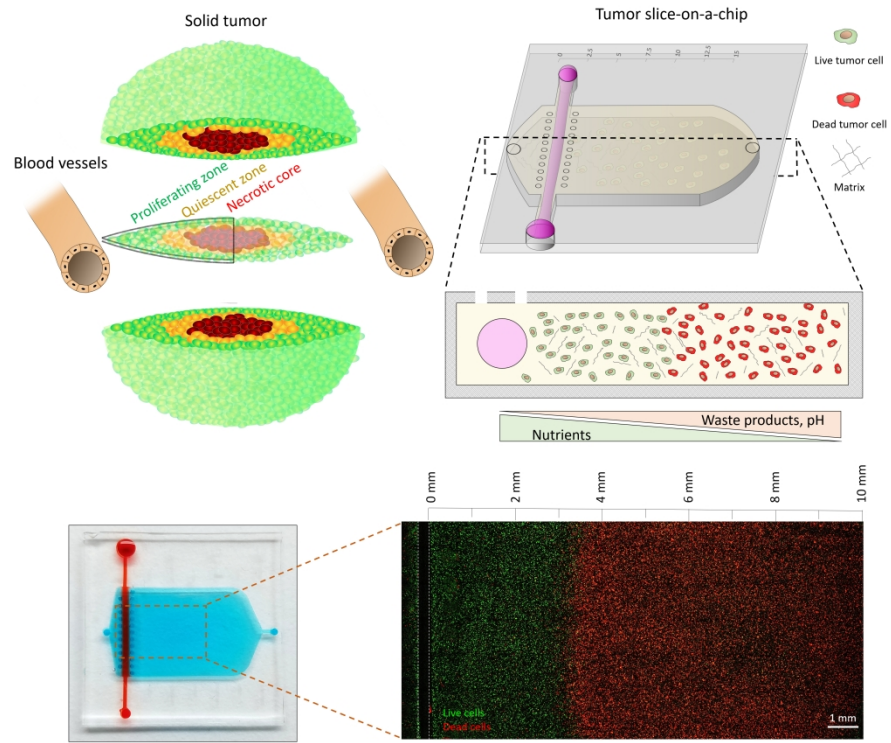


Figure 7. Spatially-controlled cell isolation and gene profiling. A) HCT-116 cells were cultured in the device at 5 million cells/ml. The modular nature of the device allowed disassembly of the top and bottom halves, exposing the hydrogel with the cells. Using a biopsy punch (1 mm diameter), fragments of the hydrogel were isolated at 0, 5 and 10 mm from the lumen. B) Hydrogel punches were degraded by collagenase type 1 in 1 min and viable and dead cells were immediately stained in green (CAM) and red (PI) respectively. C) The graph shows cell viability was larger than 90% at 0 and 10 mm immediately after recovering the cells. D) The gene expression of ninety genes was analyzed at the three different location (i.e., 0, 5 and 10 mm from the lumen) and the data was analyzed by a non-hierarchical clustering, displaying the data as a heatmap with dendrograms. The analysis revealed the punches at 5 and 10 mm were more similar compared with the 0 mm punch. E) The waterfall graph shows the fold change normalized mRNA expression for the genes differentially expressed at 0, 5 and 10 mm (blue, green and red).

605x347mm (150 x 150 DPI)



Graphical abstract

730x583mm (150 x 150 DPI)